Journal of Sol-Gel Science and Technology (2021) 99:178–187
https://doi.org/10.1007/s10971-021-05557-3

ORIGINAL PAPER: SOL-GEL AND HYBRID MATERIALS FOR BIOLOGICAL AND HEALTH (MEDICAL)

Synthesis and characterization of ultrafine γ-Al_2O_3:Cr nanoparticles and their performance in antibacterial activity

Merat Karimi[1] · Mohammad Almasi Kashi[1,2] · Amir H. Montazer[1]

Received: 15 February 2021 / Accepted: 18 May 2021 / Published online: 3 June 2021

Abstract

Preventing the growth of potentially deadly bacteria by newly synthesized nanoparticles (NPs) is of great importance in the development of future drugs. Here, chromium-doped alumina (Al_2O_3:Cr) NPs with an average diameter of about 6 nm were synthesized by a novel combination of chemical and sol–gel methods, followed by their calcination at different temperatures. The antibacterial properties of the resulting non-porous NPs were evaluated by the decomposition of two detectors (anthracene and methylene blue), and biofilms with five different concentrations (0−100 mg/mL), while also investigating structural, chemical, morphological and optical properties. Scanning and transmission electron microscopic analyses, along with X-ray diffraction patterns of the Al_2O_3:Cr NPs revealed ultrafine crystalline particulates with spherical-like morphology. Moreover, the formation of Al–O chemical bonds, and an optical band gap of 3.07 eV were evidenced. Antibacterial activity of the γ-Al_2O_3:Cr NPs calcined at 800 °C showed high inhibitions of 60% and 61% against *S.aureus* and *P.aeruginosa* microorganisms at a minimum inhibitory concentration of 100 mg/mL, indicating their potential use in the decomposition of gram-positive and gram-negative biofilms, respectively.

Graphical Abstract

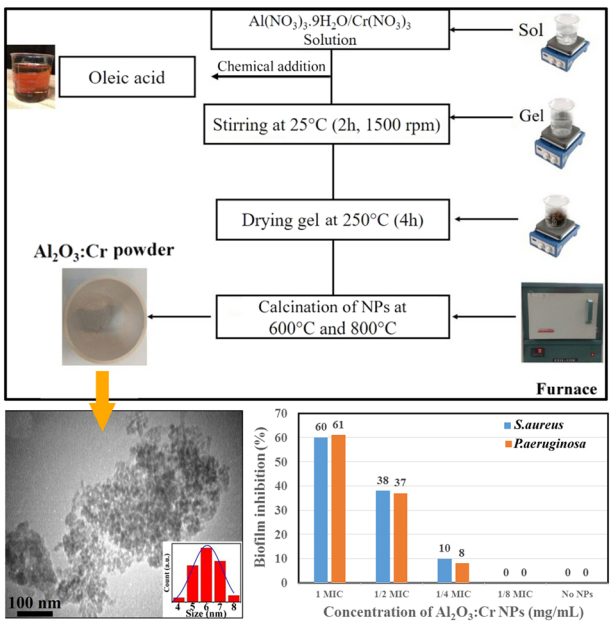

✉ Mohammad Almasi Kashi
almac@kashanu.ac.ir

[1] Institute of Nanoscience and Nanotechnology, University of Kashan, Kashan 87317−51167, Iran

[2] Department of Physics, University of Kashan, Kashan 87317−51167, Iran

Keywords γ-Al_2O_3:Cr nanoparticles · Chemical method · Sol–gel method · Reactive oxygen species · Antibacterial activity

Highlights

- Ultrafine γ-Al_2O_3:Cr nanoparticles were synthesized by a combination of chemical and sol–gel methods.
- Crystalline, compositional, morphological, chemical state, and optical properties were investigated.
- Antibacterial activity of the nanoparticles calcined at 800 °C was tested against two microorganisms.
- Biofilm decomposition with high inhibitions of 60% and 61% was obtained against *S.aureus* and *P.aeruginosa*.

1 Introduction

Bacterial diseases are a worldwide problem for the human health, and are among the main reasons for human mortality, leading to considerable damage to human society [1, 2]. Despite all the advances made in this regard, most of the mortality of patients is due to bacterial invasion, attacking some certain organs such as the brain, lungs, bones, and liver [3, 4]. As well, traditional antibacterial treatments including the use of antibiotics may develop antibiotic resistance, threatening the health of humans and animals [5–7]. In the past decades, broad strategies involving nanodrugs have been adopted to cure bacterial diseases based on antibiotic-free treatments [8, 9]. These achievements may lead to an increase in the survival rate of patients.

Notably, photodynamic therapy may be considered a clinical treatment of bacterial diseases [10, 11], consisting of the following three main parts: the material sensitive to the light, the light with a certain wavelength, and the oxygen molecule. When these parts combine with each other, reactive oxygen groups are induced. Various incident lights such as X-ray and infrared have been used in order to enhance the photodynamic therapy effect when two photons are combined together [12]. On the other hand, depending on the material sensitive to light and the incident light energy, the mechanism involved in the mortality by bacteria will be different [13, 14]. The production and design of different light-sensitive materials cause more wavelengths and singlet oxygen regions to be active, leading to shorter periods of sensitivity elimination [14, 15].

Essentially, the photodynamic therapy is based on the certain energy of the photoactivity of absorbed molecules, producing reactive oxygen species to kill damaged cells [16]. The production of these species is performed through two photochemical mechanisms. The first mechanism involves the absorption of hydrogen atoms or the electron transfer between the excited light-sensitive atoms in the triplet state, or proximity of one of organic molecules or excited oxygen molecules in a micron-size cell texture to form radicals and superoxide anions (O_2^-) [17].

In turn, the superoxide anions may be combined with each other to generate hydrogen peroxide (H_2O_2). Hydrogen peroxide and superoxide anions with high concentrations may produce hydroxyl radical (OH^-) as well. In the second mechanism, singlet oxygen ($^1O_2$) is generated with the energy transition from excited light-sensitive atoms in the triplet state to oxygen molecules during the collision process [17]. For better clarity, the aforementioned photochemical mechanisms are schematically depicted in Fig. 1

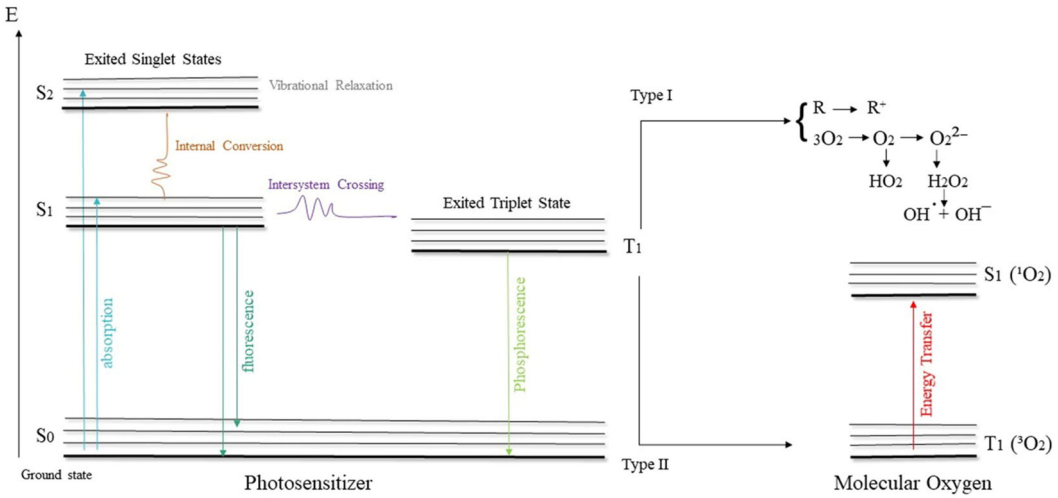

Fig. 1 Schematic representation of the production of reactive oxygen species by two photochemical mechanisms

[18]. In the photodynamic therapy, the photochemical process of both methods occurs simultaneously, whose ratios depend on the light-sensitive material employed, available oxygen and organic materials.

Nanoparticles (NPs) are commonly used in the photodynamic therapy in order to increase the death rate of bacterial cells, and make the emitting region more effective for sensitivity elimination [16]. They can also increase the capability of encapsulating light-sensitive materials, keeping them in monomeric templates. The solubility of light-sensitive materials may be enhanced after adding NPs, producing extra singlet oxygen molecules [19]. Metal-oxide NPs such as Al_2O_3, ZnO, TiO_2, and CuO are known to have good antibiotic and antimicrobial properties, widely affecting microorganisms [20–23].

It is possible to employ an optimum amount of light-sensitive materials for photodynamic therapy, thus designing applicable composites through combining various sensitizers with different types of chemotherapy medicines, and achieving photodynamic therapy with directive imaging by multimolecular agents [16]. NPs acting as light-sensitive materials have also many advantages in drug delivery systems, including the biocompatible production of photosensitizers against enzyme decomposition, and control of the release of photosensitizers in target tissues [19]. In addition, metal NPs (e.g., Au, Ag and Cu NPs) have shown good medicinal properties in treating bacteria-based diseases [24–26].

Alumina (Al_2O_3) is a common industrial catalyst with relatively uniform and high surface area mesopores, providing large thermal stability compared to other mesoporous materials [27, 28]. Apart from their special properties, Al_2O_3 NPs are a good candidate for carrying drugs, and have other applications in thermal sensors and catalyst supports [20, 29]. Other advantages of Al_2O_3 NPs include low toxicity, low price and various surface modifications [29]. The band gap energy of pure Al_2O_3 NPs ($E_g \sim$ 3.43 eV) [30] is also suitable for photodynamic applications. Recent research investigations have focused on the doping of Al_2O_3 NPs with different elements such as Ag [31], and Co [32] in order to enhance antibacterial and photocatalytic activity properties, involving improved activities of surface plasmonics, reactive oxygen species and photosensitivity. Chromium (Cr)-doped alumina (Al_2O_3:Cr) NPs have also been synthesized using combustion and solid-state methods, and their electrical, optical and structural properties have been investigated [33, 34]. To the best of our knowledge, however, no attention has so far been paid to the antibacterial activity of Al_2O_3:Cr NPs.

In this paper, by combining chemical and sol–gel methods, extremely small (ultrafine; <10 nm) γ-Al_2O_3:Cr NPs are synthesized at different calcination temperatures. The resulting NPs are then characterized in terms of crystal structure, composition, morphology, and optical absorption. In order to evaluate the ability of the Al_2O_3:Cr NPs to produce reactive oxygen species, the absorption and emission spectra of two detectors (anthracene and methylene blue) are investigated. Moreover, the NPs are employed for studying the decomposition of gram-positive and gram-negative bacterial biofilms. This study provides evidence on beneficial employment of γ-Al_2O_3:Cr NPs for antibacterial properties.

2 Experimental details

2.1 Synthesis of Al_2O_3:Cr NPs

Al_2O_3:Cr NPs were synthesized using a combination of chemical and sol–gel methods. In this regard, aluminum nitrate [$Al(NO_3)_3{\cdot}9H_2O$, 99%], oleic acid ($C_{18}H_{34}O_2$, 99%), and chromium nitrate [$Cr(NO_3)_3$, 99%] were purchased from Merck, and used without further purification.

1.875 g of $Al(NO_3)_3{\cdot}9H_2O$ was mixed with 1 mole% of $Cr(NO_3)_3$ in 20 ml of deionized water, and the resultant solution was placed on a magnetic stirrer to homogenize it during 30 min at room temperature (25 °C), thus obtaining the sol. In the following, 20 ml of oleic acid with a volume ratio of 1:1 was added to the solution of the mixture, and it was placed on a magnetic stirrer (1500 rpm) for 2 h at 25 °C. To evaporate the remaining water, the solution was heated to the temperature of 250 °C for 4 h, thereby transforming it into a black gel. Finally, the whole black gel was calcined at different temperatures (600 °C and 800 °C) for 2 h to form Al_2O_3:Cr powder. For better clarity, Fig. 2 shows a diagram

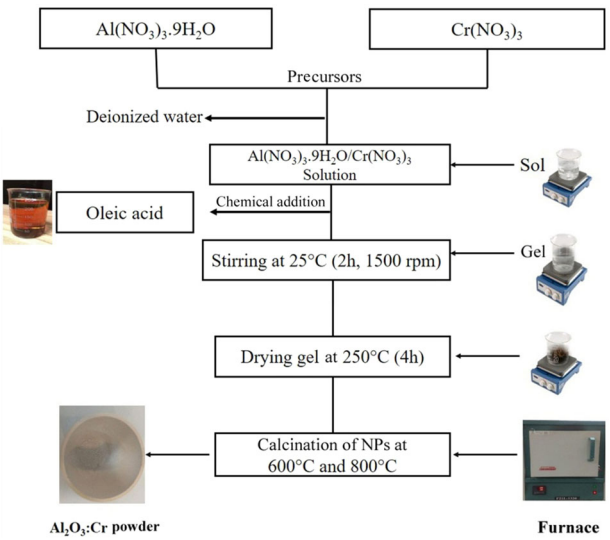

Fig. 2 The diagram of the synthesis of Al_2O_3:Cr NPs using a combination of chemical and sol–gel methods

of the synthesis of Al_2O_3:Cr NPs using the combination of chemical and sol–gel methods.

2.2 Characterizations

Crystal structure was investigated using X-ray diffraction (XRD; model: Philips X'pert Pro MPP with Cu Kα radiation filtered by Ni, and $\lambda = 0.1540$ nm) analysis. In this regard, the average crystallite size (D) of Al_2O_3:Cr NPs was estimated based on the Scherrer formula as given below [35]:

$$D = \frac{K\lambda}{\beta COS\theta} \quad (1)$$

where k is the shape factor ($k = 0.9$), λ is the wavelength of the incident beam, β is the full width at half maximum, and θ is the incident beam angle.

Morphology, composition and particle size of the NPs were determined by a scanning electron microscope (SEM; model: TESCAN Mira 3–XMU) equipped with an energy-dispersive spectrometer (EDS), and a transmission electron microscope (TEM; model: Zeiss EM900). The dynamic light scattering (Vasco/Cordouan Technologies/France) method [36] was also carried out to identify size distribution of the NPs.

A Fourier transform infrared (FT-IR; model: Magna–IR550) spectrometer was used to investigate the presence of functional groups. The FT-IR samples were prepared using the KBr pellet technique. An ultraviolet–visible (UV–Vis; UVS-2500, Phystech) spectrometer was used in the range of 200−800 nm in order to investigate optical properties at room temperature. In this case, anthracene and methylene blue were employed as detectors due to their high availability and low price.

2.3 Antibacterial activity and biofilm formation tests

Antibacterial activity of γ-Al_2O_3:Cr nanoparticles was tested by measuring minimum inhibitory concentration (MIC), and minimum bacterial concentration (MBC) using a micro-well dilution method for two microorganisms (*P.aeruginosa* and *S.aureus*). To determine MIC of the growth of the microorganisms, sterilized 96-well microplates were initially prepared. 96 µL of culture medium, 5 µL of bacterial suspension with a concentration of 0.5 McFarland, and 100 µL of different concentrations of Al_2O_3:Cr NPs were then added to each plate.

Afterwards, the plate was heated in an incubator at 37 °C for 24 h. The micro dilution method was carried out in the highest concentration of the NPs, ranging from 1000 µg/ml to less than 15.63 µg/ml, and each concentration was half of the previous one. To determine the MBC after 24 h of heating, 5 µL of each microplate well (without bacterial growth) was incorporated into the nutrient agar medium, and exposed to heat at 37 °C for 24 h.

The evaluation of the ability of the microorganisms (bacteria) to form a biofilm was also carried out by 96-well microplates. To this end, the bacteria used in the tryptic soy broth (TSB) culture medium were kept at 37 °C for 24 h. In each row (comprising 12 wells) of the microplate, 8 wells were dedicated to each bacterium, and the remaining 4 wells were dedicated to the negative control containing 200 µL of pure TSB without bacterium. 100 µL of the diluted suspension of 6 bacteria with a concentration of 10 ml/CFU together with 100 µL of the TSB culture medium was poured into each well. In continuance, the microplate was placed at a temperature of 37 °C for 24 h. The microplates were then reversed to empty the wells from the existing culture medium. Afterwards, the wells were rinsed three times with sterilized phosphate buffer to eliminate the bacteria that had not formed a biofilm. To dry the microplates, they were left upside-down at room temperature for 1 h. Next, 200 µL of 2 wt.% crystal violet solution was added to each well, and the microplate was place at 37 °C for 15 min. The dye in the wells was then removed, and the microplates were dried at room temperature after rinsing them with sterilized phosphate buffer. To extract the dye bonded to the bacteria forming biofilms, 200 µL of 30 wt.% acetic acid was added to each well. Using a microplate reader, the optical absorption of the resulting solution was measured at 595 nm, while also evaluating the ability of the bacteria to form a biofilm, according to the method explained above.

Basically, biofilms are complex matrices of microorganisms attached to surfaces [37]. In this study, two microorganisms were employed: the *S.aureus* microorganism as a gram-positive bacterium whose cell division takes place in more than one direction, and the *P.aeruginosa* as a gram-negative bacterium with a polar mobile flagellum leading to nosocomial infections in weakened immune system [38]. The source for the growth of these microorganisms is the nose hole [39].

The intrinsic resistivity against antibiotics and detergent materials is the most important factors that can cause these bacteria to be infectious. Therefore, new methods for controlling biofilms have recently been developed based on the synthesis of NPs with different sizes and morphologies. In other words, the small size and the high surface area of NPs lead to enhanced evolution of chemical, biological and antimicrobial properties. Furthermore, the solubility and high mobility of NPs enable them to enter into the cell membrane of the human body easily [36, 40].

In general, since bacteria cells have many acidic structures, their biological pH is measured to be negative, leading to the negative charge of cell walls when they are separated from each other [41]. Metal oxide NPs can be

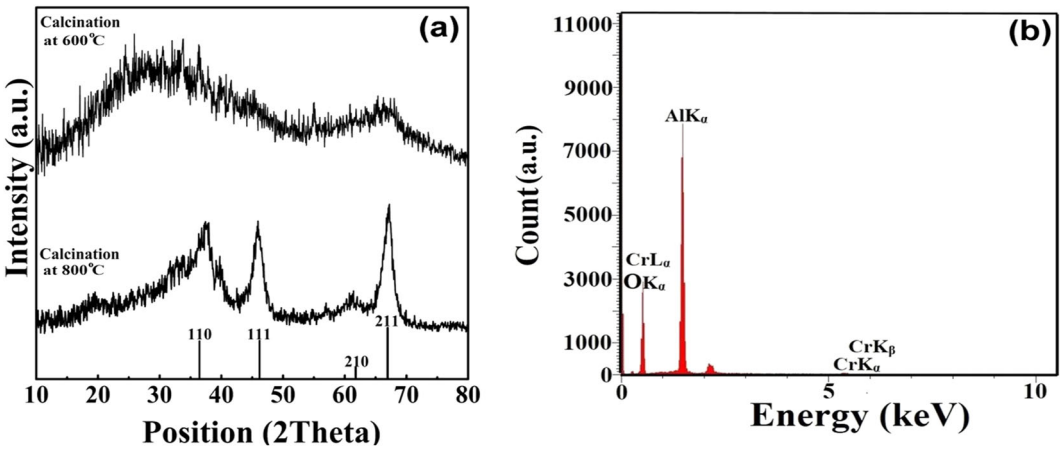

Fig. 3 **a** XRD patterns of Al_2O_3:Cr NPs calcined at 600 and 800 °C. **b** EDS spectrum of Al_2O_3:Cr NPs calcined at 800 °C

attached to the bacteria membranes thorough electrostatic reactions, thereby making the plasma membrane potential unstable, while also killing the bacteria [42]. This mechanism of the antibacterial activity of metal oxide NPs is based on the release of ions, and the production of inner cell reactive oxygen species. Here, the decomposition of microbial biofilms was investigated for five different concentrations: 1 MIC, $\frac{1}{2}$ MIC, $\frac{1}{4}$ MIC, $\frac{1}{8}$ MIC, and 0 MIC.

3 Results and discussion

3.1 Structure, composition, and morphology

Figure 3a shows XRD patterns of Al_2O_3:Cr NPs calcined at 600 °C and 800 °C. The former indicates that the NPs calcined at 600 °C are amorphous without any sharp diffraction peak. Increasing the calcination temperature to 800 °C leads to the emergence of a crystalline phase. Accordingly, the XRD peaks observed at $2\theta^\circ = 36.2^\circ$, 41.4°, 62.3°, and 67.8° are assigned to Al_2O_3(110), Al_2O_3(111), Al_2O_3(210), and Al_2O_3(211) planes (JCPDS card no. 00-001-1303), respectively, indicating the formation of the γ-Al_2O_3 phase with a cubic structure. The corresponding lattice parameter of the (211) plane is also found to be $a = 2.89$ Å. Moreover, the average crystallite size is obtained to be about 10 nm, and no secondary phase is observed in the XRD pattern. The absence of peaks related to the element Cr is probably due its extremely low content in the alumina compound. On the other hand, Fig. 3b shows the EDS spectrum of the γ-Al_2O_3:Cr NPs calcined at 800 °C. The presence of the elements Al, O and Cr with respective atomic percentages of 64.5, 35, and 0.5% is confirmed. The actual concentration of the Cr dopant is found to be ~1%, which is in accordance with the stoichiometric amount.

Figure 4a shows a top-view SEM image of γ-Al_2O_3:Cr NPs calcined at 800 °C. The NPs are observed to be attached together, forming a relatively continuous and uniform film on the surface. It appears that the use of the oleic acid in the chemical synthesis method can act as a surfactant, giving rise to the formation of small-size and uniform Al_2O_3:Cr NPs. To investigate the size distribution of the calcined NPs in detail, TEM analysis was employed.

Figure 4b shows a TEM image of the NPs calcined at 800 °C, together with the corresponding size distribution histogram [the inset of Fig. 4b]. As can be seen, the NPs are ultrafine, so that the size of spherical-like NPs is found to range from 4 to 8 nm. The average diameter of the γ-Al_2O_3:Cr NPs is about 6 nm. The formation of ultrafine NPs was further confirmed by the dynamic light scattering method, according to Fig. 4c. Accordingly, one can find that no considerable NP aggregation occurs in the solution.

3.2 FT-IR spectra

In the FT-IR spectroscopy, the radiation of infrared to the NP sample would lead to a change in the energy of bond vibrations, and the absorption amount is identified in terms of the wavenumber for chemical bonds. The wavenumber interval from 400 to 1500 cm^{-1} is known as the fingerprint region, revealing the occurrence of unique molecular vibrations in the NP sample [43]. Here, FT-IR spectra of the Al_2O_3:Cr NPs calcined at 600 and 800 °C were investigated in the wavenumber interval of 400−4000 cm^{-1}, and the result are shown in Fig. 5. At the calcination temperature of 600 °C, the bands at the wavenumbers of 630, 1646, and 3448 cm^{-1} are assigned to Al–O, H_2O and O–H bonds, respectively [43]. Similarly, the bands at the wavenumbers of 557, 1644, and 3459 cm^{-1} are attributed to Al–O, H_2O and O–H bonds for the Al_2O_3:Cr NPs calcined at 800 °C, respectively [43]. Therefore, the calcination temperature has

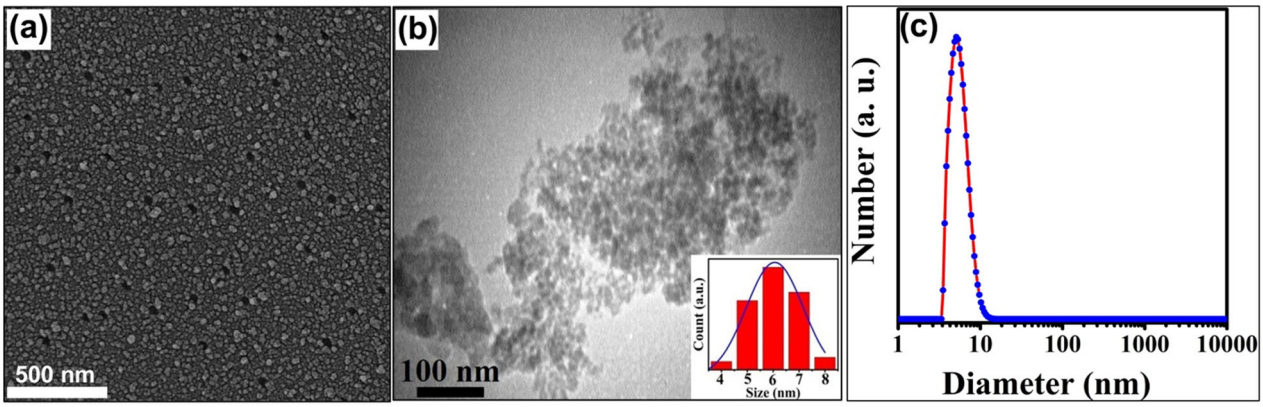

Fig. 4 **a** Top-view SEM image, **b** TEM image, and **c** dynamic light scattering spectrum of γ-Al_2O_3:Cr NPs calcined at 800 °C. The inset in part **b** shows the corresponding size distribution histogram

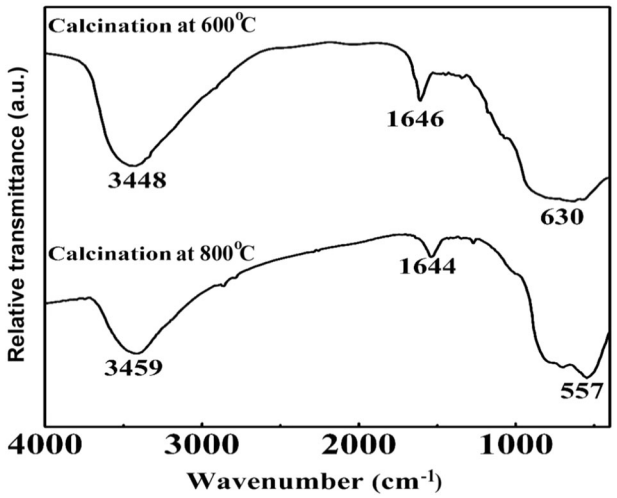

Fig. 5 FT-IR spectra of Al_2O_3:Cr NPs calcined at 600 and 800 °C

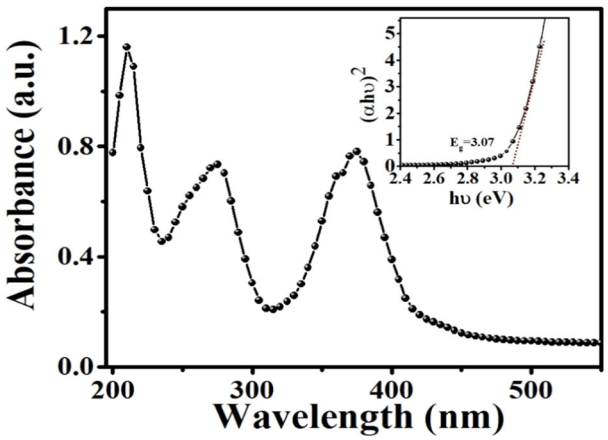

Fig. 6 The UV–Vis spectrum of γ-Al_2O_3:Cr NPs calcined at 800 °C. The inset shows the corresponding optical band gap calculation

no considerable effect on the FT-IR spectra. Note that the shift in the peak from 630 to 557 cm^{-1} may occur due the formation of the γ-Al_2O_3 crystalline phase at 800 °C, as evidenced from the corresponding XRD pattern [see Fig. 3a].

3.3 Optical properties

UV–Vis spectroscopy enables us to measure the absorption wavelength based the interaction of the light with the NP samples. Figure 6 shows the UV–Vis spectrum of the γ-Al_2O_3:Cr NPs calcined at 800 °C.

Evidently, the resulting NPs show strong absorption peaks at the wavelengths of 210, 275 and 379 nm, likely arising from the intrinsic defects in the NPs, and the presence of the Cr additive [34, 44]. The corresponding optical band gap of NPs was calculated based on the Tauc method, and the result is shown in the inset of Fig. 6. In the Tauc method, it is assumed the absorption coefficient (α) is dependent on the band gap energy (E_g) as follows [45]:

$$(\alpha \cdot h\nu)^{1/\gamma} = B(h\nu - E_g) \quad (2)$$

where h, ν, and B are the Planck constant, photon frequency, and a constant. The parameter γ was selected to be 1/2 for the direct band gap. It is found that the γ-Al_2O_3:Cr NPs have a direct E_g of 3.07 eV, being smaller than that of pure Al_2O_3 NPs. This can be attributed to the ultrafine size of the Cr-doped Al_2O_3 NPs, according to the TEM and dynamic light scattering results [see Fig. 4b and c]. Compared to the bulk state of Al_2O_3 with E_g ~ 9 eV, the presence of defects in the band gap region can be responsible for the significantly smaller E_g of the Cr-doped NPs [46].

In order to specify the singlet oxygen, and indirectly measure the cell toxicity produced by the NPs, anthracene with the molecular formula of $C_{14}H_{10}$ was used, which can be transformed into anthraquinone during the oxidation process in the liquid or gas phase [47, 48].

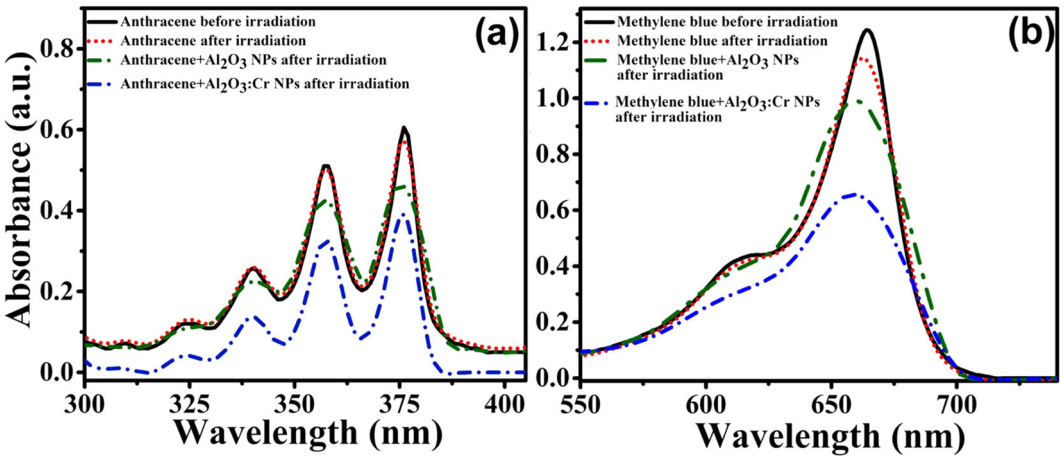

Fig. 7 The UV–Vis spectra obtained from: (**a**) anthracene solution, and (**b**) methylene blue solution without and with pure γ-Al_2O_3 and γ-Al_2O_3:Cr NPs, before and after irradiation for 1 h

By using the anthracene (acting as a fluorescent material), it is indirectly possible to evidence the production of singlet oxygen. In other words, the more singlet oxygen is produced, the more anthracene amount will be transformed into anthraquinone, which in turn reduces the absorption intensity of anthracene. A UV light beam was used to excite the NPs, and induce the oxidation process in the anthracene. The UV absorption spectra of anthracene solution with and without γ-Al_2O_3:Cr NPs were also used to investigate the detection amount of the singlet oxygen produced.

Figure 7a shows UV–Vis spectra obtained from anthracene solution without the NPs before and after irradiation for 1 h. In this case, no considerable difference is observed before and after the irradiation, indicating the incapability of the anthracene solution to produce singlet oxygen. Interestingly, the anthracene solution comprising γ-Al_2O_3:Cr NPs shows enhanced emission intensity due to the decomposition of anthracene, and the anthraquinone production, according to Fig. 7a. In fact, the NPs play an important role in the anthracene decomposition, leading to an increase in active sites on their surface, while also producing singlet oxygen. To provide better evidence, UV–Vis spectrum obtained from anthracene solution with pure Al_2O_3 NPs is also shown in Fig. 7a, revealing their lower emission intensity compared to the Cr-doped Al_2O_3 NPs.

On the other hand, in order to identify hydroxyl free radicals, and indirectly measure the cell toxicity produced by the NPs, methylene blue with the molecular formula of $C_{16}H_{18}N_3SCl$ was used. Methylene blue is highly soluble in water (H_2O), and shows good optical stability against the UV light. It is decomposed during the oxidation reaction in the presence of hydroxyl free radicals, thereby being transformed into H_2O and carbon dioxide (CO_2) [49, 50]. Since the emission spectrum of methylene blue is in the range of the visible light, it is easy to observe a decrease in the emission or absorption intensity when fading its color.

A UV light beam was used to investigate the detection amount of hydroxyl free radical in methylene blue solution without and with γ-Al_2O_3:Cr NPs, and the results are shown in Fig. 7b. As inferred, while irradiation of 1 h to the methylene blue solution without the NPs can slightly influence its absorption, the addition of Cr-doped Al_2O_3 NPs significantly reduces the absorption intensity. In turn, this indicates the production of free radicals due to the methylene blue decomposition. For better evidence, Fig. 7b shows UV–Vis spectrum of methylene blue solution with pure Al_2O_3 NPs, indicating their higher absorption intensity compared to the Cr-doped Al_2O_3 NPs. Overall, the enhanced production of singlet oxygen and free radicals may be indicative of the potential applicability of the γ-Al_2O_3:Cr NPs for antibacterial activity, which is discussed in the next Section

3.4 Antimicrobial activity

The γ-Al_2O_3:Cr NPs synthesized by the combination of chemical and sol–gel methods were tested against two microorganisms as described in the experimental details, and the results of MIC and MBC are tabulated in Table 1. Notably, the respective minimum−maximum MIC and MBC of the *P.aeruginosa* microorganism are found to be 13.00−13.10 and 26.00−26.50 mg/mL, indicating good antibacterial activity. To better understand the effect of the Cr doping on the antibacterial activity, pure γ-Al_2O_3 NPs were also tested against the *S.aureus* and *P.aeruginosa* microorganisms, and the results of MIC and MBC are tabulated in Table 2. As can be seen, significantly higher MIC and MBC concentrations of the Al_2O_3 NPs are needed to inhibit the growth of the bacteria compared to those of

Table 1 MIC and MBC for standard stains of *S.aureus* ATCC 43300, and *P.aeruginosa* PAO1 by using γ-Al_2O_3:Cr NPs

Microorganism	NPs: γ-Al_2O_3: Cr			
	MIC		MBC	
	Minimum−Maximum (mg/mL)	Mean ± SD	Minimum−Maximum (mg/mL)	Mean ± SD
S.aureus ATCC 43300	13.00−13.10	13.03 ± 0.057	26.00	26.00
P.aeruginosa PAO1	13.00−13.10	13.50 ± 0.050	26.00−26.50	26.15 ± 0.26

SD standard deviation

Table 2 MIC and MBC for standard stains of *S.aureus* ATCC 43300, and *P.aeruginosa* PAO1 by using pure γ-Al_2O_3 NPs

Microorganism	NPs: γ-Al_2O_3			
	MIC		MBC	
	Minimum−Maximum (mg/mL)	Mean ± SD	Minimum−Maximum (mg/mL)	Mean ± SD
S.aureus ATCC 43300	237.5−262.5	250 ± 12.5	1000.00−1050.00	950.00 ± 50.00
P.aeruginosa PAO1	14.84−16.4	15.63 ± 0.78	1000.00−1050.00	950.00 ± 50.00

SD standard deviation

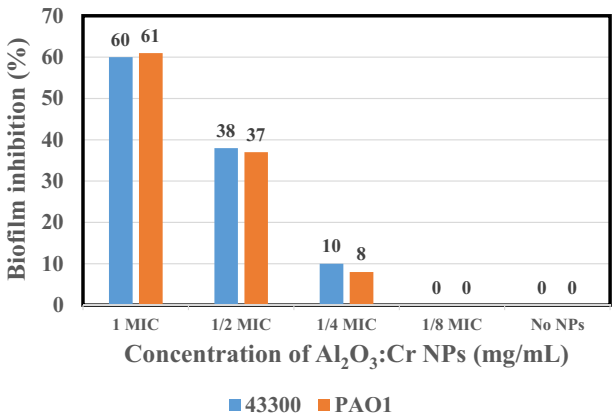

Fig. 8 Biofilm inhibition of Al_2O_3:Cr NPs with different concentrations against standard stains of *S.aureus* ATCC 43300, and *P. aeruginosa* PAO1

Cr-doped Al_2O_3 ones. Therefore, γ-Al_2O_3:Cr NPs outperform the pure γ-Al_2O_3 NPs in terms of antibacterial activity.

Alternatively, Fig. 8 shows the biofilm inhibition of Al_2O_3:Cr NPs with different concentrations against standard stains of *S.aureus* ATCC 43300, and *P.aeruginosa* PAO1. Increasing the NP concentration beyond $\frac{1}{8}$ MIC starts to decompose the biofilms, reaching respective inhibitions of 10% and 8% against *S.aureus* and *P.aeruginosa* microorganisms at $\frac{1}{4}$ MIC. This arises due to the enhanced production of reactive oxygen species when increasing the concentration of NPs. The highest inhibitions are achieved to be 60% and 61% using a concentration of 1 MIC against the aforementioned microorganisms, according to Fig. 8. Gomez-Polo et al. [51] have recently investigated the effect of Cr doping on antibacterial activity of TiO_2 NPs synthesized using a sol–gel method. They examined the antibacterial response of the TiO_2:Cr NPs against *Escherichia coli* DH5α strain under darkness and visible light, demonstrating that the Cr-doped NPs with slight toxicity show perceptible antibacterial performance under the irradiation of visible light [51]. Thus, the TiO_2:Cr NPs need visible light to show antibacterial activity, whereas the good antibacterial performance of the γ-Al_2O_3:Cr NPs in the present study was obtained without the illuminated conditions. Elsewhere, antibacterial activity of chromium oxide (Cr_2O_3) NPs against gram-negative and gram-positive bacteria, including *E.coli*, *B.sps* and *S.aureus* has been studied, resulting in maximum inhibition of 15 mm [52]. Moreover, using an electrodeposition process, Ag NPs have been coated with Cr, followed by evaluating their antibacterial activity against gram-positive *S.aureus* and gram-negative *E.coli* bacteria [53]. In this case, the composite coatings of Cr/Ag NPs inhibited the growth of *S.aureus* and *E.coli* bacteria up to 99.92 and 99.98%, respectively. Overall, one can conclude that Cr can be used as an effective dopant or coating material in inhibiting the growth of various gram-negative and gram-positive bacteria, thus potentially constituting promising commercialized nanodrug candidates in a foreseeable future.

4 Conclusions

In conclusion, Al_2O_3:Cr NPs were synthesized by combining the chemical (using oleic acid) and sol–gel methods, and subsequently calcined at 600 and 800 °C. The XRD and EDS analyses evidenced the formation of the γ-Al_2O_3 phase in the NPs with an average crystallite size of 10 nm doped with the element Cr with a content of about 1% and calcined at 800 °C. The SEM and TEM investigations revealed the

formation of relatively uniform and ultrafine spherical-like NPs with sizes ranging from 4 to 8 nm. On the other hand, the FT-IR and UV–Vis investigations showed the formation of Al–O bonds for γ-Al_2O_3:Cr NPs with a band gap energy of 3.07 eV. Moreover, UV–Vis spectra obtained from anthracene and methylene blue solutions containing the NPs showed a significant decrease in the emission intensity, indicating the enhanced production of single oxygen and hydroxyl free radicals after irradiation for 1 h. By investigating antibacterial performance, the Cr-doped Al_2O_3 NPs resulted in good antibacterial activity by showing high minimum-maximum MIC and MBC (e.g., 13.00−13.10 and 26.00−26.50 against *P.aeruginosa*). Increasing the NP concentration beyond $\frac{1}{8}$ MIC continuously enhanced the biofilm decomposition, resulting in high inhibition (e.g., 60% against *S.aureus*) at 1 MIC.

Data availability

The data will be available upon request.

Funding The authors gratefully acknowledge the University of Kashan for providing the financial support of this research by Grant no. 159023/76.

Compliance with ethical standards

Conflict of interest The authors declare no competing interests.

Consent for publication By submitting the manuscript, the authors understand that the material presented in this manuscript has not been published before, nor has it been submitted for publication to another journal. The corresponding author attests that this study has been approved by all the co-authors concerned.

Publisher's note Springer Nature remains neutral with regard to jurisdictional claims in published maps and institutional affiliations.

References

1. Kwon YS, Park SH, Kim M-A, Kim HJ, Park JS, Lee MY et al. (2017) Risk of mortality associated with respiratory syncytial virus and influenza infection in adults. BMC Infect Dis 17:1–9
2. Gupta A, Patel SS, Langute SM, Kolkar M, Hemamalini H, Shinde SK et al. (2017) Bacterial diseases of livestock animals and their impact on human health. Innovare J Sci 5:8–11
3. R Mirzaei, R Mohammadzadeh, M Sholeh, S Karampoor, M Abdi, E Dogan, et al. (2020) The importance of intracellular bacterial biofilm in infectious diseases, Microb Pathog 147:104393
4. Principi N, Esposito S (2020) Bacterial meningitis: new treatment options to reduce the risk of brain damage. Expert Opin Pharm 21:97–105
5. Xue X, Jia J, Yue X, Guan Y, Zhu L, Wang Z (2021) River contamination shapes the microbiome and antibiotic resistance in sharpbelly (Hemiculter leucisculus). Environ Pollut 268:115796
6. Andrade GF, Faria JAQA, Gomes DA, de Barros ALB, Fernandes RS, Coelho ACS et al. (2018) Mesoporous silica SBA-16/hydroxyapatite-based composite for ciprofloxacin delivery to bacterial bone infection. J Sol-Gel Sci Techn 85:369–381
7. Tan Q, Li W, Zhang J, Zhou W, Chen J, Li Y et al. (2019) Presence, dissemination and removal of antibiotic resistant bacteria and antibiotic resistance genes in urban drinking water system: a review. Front Environ Sci Eng 13:1–15
8. Syed MA, Ali N (2019) Nanomaterials for selective targeting of intracellular pathogens, in nanotheranostics, Springer, Switzerland pp. 115–136
9. Bueno J (2020) Antimicrobial nanotechnology in preventing the transmission of infectious disease, in preclinical evaluation of antimicrobial nanodrugs, Springer, Switzerland pp. 75–88
10. Yu Q, Huang T, Liu C, Zhao M, Xie M, Li G et al. (2019) Oxygen self-sufficient NIR-activatable liposomes for tumor hypoxia regulation and photodynamic therapy. Chem Sci 10:9091–9098
11. Alves F, Gomes Guimarães G, Mayumi Inada N, Pratavieira S, Salvador Bagnato V, Kurachi C (2021) Strategies to Improve the Antimicrobial Efficacy of Photodynamic, Sonodynamic, and Sonophotodynamic Therapies. Lasers Surg Med. https://doi.org/10.1002/lsm.23383
12. Bakhmetyev VV, Dorokhina AM, Keskinova MV, Mjakin SV, Vlasenko AB, Lebedev LA et al. (2020) Synthesis and characterization of finely dispersed phosphors doped with rare-earth metal ions for enhanced photodynamic therapy of cancer. Chem Pap 74:787–797
13. Janani M, Jafari F, Samiei M, Lotfipour F, Nakhlband A, Ghasemi N et al. (2017) Evaluation of antibacterial efficacy of photodynamic therapy vs. 2.5% NaOCl against E. faecalis-infected root canals using real-time PCR technique. J Clin Exp 9:e539
14. Mazur LM, Roland T, Leroy-Lhez S, Sol V, Samoc M, Samuel ID et al. (2019) Efficient singlet oxygen photogeneration by zinc porphyrin dimers upon one-and two-photon excitation. J Phys Chem B 123:4271–4277
15. Zhang J, Jiang C, Longo JPF, Azevedo RB, Zhang H, Muehlmann LA (2018) An updated overview on the development of new photosensitizers for anticancer photodynamic therapy. Acta Pharm Sin B 8:137–146
16. Shen Y, Shuhendler AJ, Ye D, Xu J-J, Chen H-Y (2016) Two-photon excitation nanoparticles for photodynamic therapy. Chem Soc Rev 45:6725–6741
17. Dąbrowski JM (2017) Reactive oxygen species in photodynamic therapy: mechanisms of their generation and potentiation. Adv Inorg Chem 70:343–394
18. Lasorne B, Worth GA, Robb MA (2011) Excited-state dynamics. Wiley Interdiscip Rev Comput Mol Sci 1:460–475
19. Lucky SS, Soo KC, Zhang Y (2015) Nanoparticles in photodynamic therapy. Chem Rev 115:1990–2042
20. He Y, He J, Zhang H, Liu Y, Lei B (2017) Luminescent properties and energy transfer of luminescent carbon dots assembled mesoporous Al2O_3: Eu3+ co-doped materials for temperature sensing. J Colloid Interface Sci 496:8–15
21. Rajakumar G, Rahuman AA, Roopan SM, Khanna VG, Elango G, Kamaraj C et al. (2012) Fungus-mediated biosynthesis and characterization of TiO_2 nanoparticles and their activity against pathogenic bacteria. Spectrochim Acta A Mol Biomol Spectrosc 91:23–29
22. Soria-Castro M, De la Rosa-García S, Quintana P, Gómez-Cornelio S, Sierra-Fernandez A, Gómez-Ortíz N (2019) Broad spectrum antimicrobial activity of Ca (Zn (OH) 3) 2· 2H2O and ZnO nanoparticles synthesized by the sol–gel method. J Sol Gel Sci Technol 89:284–294
23. Magyari K, Pap Z, Tóth Z-R, Kása Z, Licarete E, Vodnar D et al. (2019) The impact of copper oxide nanoparticles on the structure

and applicability of bioactive glasses. J Sol Gel Sci Technol 91:634–643
24. Karthik S, Suriyaprabha R, Vinoth M, Srither S, Manivasakan P, Rajendran V et al. (2017) Larvicidal, super hydrophobic and antibacterial properties of herbal nanoparticles from Acalypha indica for biomedical applications. RSC Adv 7:41763–41770
25. Wang S, Wang Y, Peng Y, Yang X (2019) Exploring the antibacteria performance of multicolor Ag, Au, and Cu nanoclusters. ACS Appl Mater Interfaces 11:8461–8469
26. Guan G, Win KY, Yao X, Yang W, Han MY (2021) Plasmonically modulated gold nanostructures for photothermal ablation of bacteria. Adv Healthc Mater 10:2001158
27. Hatamie S, Ahadian MM, Rashidi A, Karimi A, Akhavan O (2017) Novel synthesis of cobalt/poly vinyl alcohol/gamma alumina nanocomposite for catalytic application. Appl Phys A 123:341
28. Shao-Hao L, Yi-Bo C, Li N, Su H, Shi-Heng G (2018) Novel gC3N4 wrapped γ-Al2O3 microspheres heterojunction for efficient photocatalytic application under visible light irradiation. J Mater Sci Mater Electron 29:4509–4516
29. Deshmukh K, Ahamed MB, Deshmukh RR, Pasha SK, Sadasivuni KK, Polu AR et al. (2017) Newly developed biodegradable polymer nanocomposites of cellulose acetate and Al2O3 nanoparticles with enhanced dielectric performance for embedded passive applications. J Mater Sci Mater Electron 28:973–986
30. Patra AK, Dutta A, Bhaumik A (2012) Self-assembled mesoporous γ-Al2O3 spherical nanoparticles and their efficiency for the removal of arsenic from water. J Hazard Mater 201:170–177
31. Lozhkomoev A, Kazantsev S, Pervikov A, Fomenko A, Gotman I (2019) New approach to production of antimicrobial Al2O3-Ag nanocomposites by electrical explosion of two wires. Mater Res Bull 119:110545
32. Anbarasu S, Ilangovan S, Usharani K, Prabhavathi A, Suganya M, Karthika M et al. (2020) Realization of improved visible light-mediated photocatalytic activity of Al2O3 nanoparticles through cobalt doping. J Electron Mater 49:869–879
33. Kakooei S, Rouhi J, Mohammadpour E, Alimanesh M, Dehzangi A (2012) Synthesis and characterization of Cr-doped Al2O3 nanoparticles prepared via aqueous combustion method. Casp J Appl Sci Res 1:16–22
34. Nguyen DK, Lee H, Kim I-T (2017) Synthesis and thermochromic properties of Cr-doped Al2O3 for a reversible thermochromic sensor. Materials 10:476
35. Manikandan B, Endo T, Kaneko S, Murali K, John R (2018) Properties of sol gel synthesized ZnO nanoparticles. J Mater Sci Mater Electron 29:9474–9485
36. Moradipour M, Chase EK, Khan MA, Asare SO, Lynn BC, Rankin SE et al. (2020) Interaction of lignin-derived dimer and eugenol-functionalized silica nanoparticles with supported lipid bilayers. Colloids Surf B Biointerfaces 191:111028
37. Mah T-FC, O'Toole GA (2001) Mechanisms of biofilm resistance to antimicrobial agents. Trends Microbiol 9:34–39
38. Craig L, Pique ME, Tainer JA (2004) Type IV pilus structure and bacterial pathogenicity. Nat Rev Microbiol 2:363–378
39. Bokarewa MI, Jin T, Tarkowski A (2006) Staphylococcus aureus: staphylokinase. Int J Biochem Cell Biol 38:504–509
40. Ghaemy M, Naseri M (2012) Synthesis of chitosan networks: swelling, drug release, and magnetically assisted BSA separation using Fe_3O_4 nanoparticles. Carbohydr Polym 90:1265–1272
41. Bosetti M, Massè A, Tobin E, Cannas M (2002) Silver coated materials for external fixation devices: in vitro biocompatibility and genotoxicity. Biomaterials 23:887–892
42. Beranová J, Seydlová G, Kozak H, Benada O, Fišer R, Artemenko A et al. (2014) Sensitivity of bacteria to diamond nanoparticles of various size differs in gram-positive and gram-negative cells. FEMS Microbiol Lett 351:179–186
43. Adamczyk A, Długoń E (2012) The FTIR studies of gels and thin films of Al2O3–TiO_2 and Al2O3–TiO_2–SiO_2 systems. Acta A Mol Biomol Spectrosc 89:11–17
44. Ayari F, Mhamdi M, Delahay G, Ghorbel A (2010) Sol–gel derived mesoporous Cr/Al2O3 catalysts for SCR of NO by ammonia. J Porous Mater 17:265–274. 2010/06/01
45. Makuła P, Pacia M, Macyk W (2018) How to correctly determine the band gap energy of modified semiconductor photocatalysts based on UV–Vis spectra, ed: ACS Publications, United States
46. Amirsalari A, Shayesteh SF (2015) Effects of pH and calcination temperature on structural and optical properties of alumina nanoparticles. Superlattice Microst 82:507–524
47. Theurich J, Bahnemann D, Vogel R, Ehamed F, Alhakimi G, Rajab I (1997) Photocatalytic degradation of naphthalene and anthracene: GC-MS analysis of the degradation pathway. Res Chem Intermed 23:247–274
48. Bakalova R, Ohba H, Zhelev Z, Ishikawa M, Baba Y (2004) Quantum dots as photosensitizers? Nat Biotechnol 22:1360–1361
49. Trandafilović LV, Jovanović DJ, Zhang X, Ptasińska S, Dramićanin MD (2017) Enhanced photocatalytic degradation of methylene blue and methyl orange by ZnO:Eu nanoparticles. Appl Catal B Environ 203:740–752. 2017/04/01/
50. Yang Y, Xu L, Wang H, Wang W, Zhang L (2016) TiO_2/graphene porous composite and its photocatalytic degradation of methylene blue. Mater Des 108:632–639. 2016/10/15/
51. Gomez-Polo C, Larumbe S, Gil A, Muñoz D, Fernández LR, Barquín LF et al. (2021) Improved photocatalytic and antibacterial performance of Cr doped TiO_2 nanoparticles. Surf Interfaces 22:100867
52. Nivethitha PR, Rachel DCJ (2020) A study of antioxidant and antibacterial activity using honey mediated Chromium oxide nanoparticles and its characterization. Mater Today Proc. https://doi.org/10.1016/j.matpr.2020.07.187
53. Méndez-Albores A, González-Arellano SG, Reyes-Vidal Y, Torres J, Ţălu Ş, Cercado B et al. (2017) Electrodeposited chrome/silver nanoparticle (Cr/AgNPs) composite coatings: characterization and antibacterial activity. J Alloy Compd 710:302–311